Quantitative 3D Analysis of Plant Roots Growing in Soil Using Magnetic Resonance Imaging[1][OPEN]

Dagmar van Dusschoten*, Ralf Metzner, Johannes Kochs, Johannes A. Postma, Daniel Pflugfelder, Jonas Bühler, Ulrich Schurr, and Siegfried Jahnke

IBG-2: Plant Sciences, Forschungszentrum Jülich, 52425 Jülich, Germany (D.v.D, R.M., J.K., J.A.P., D.P., J.B., U.S., S.J.).

ORCID IDs: 0000-0002-6251-1231 (D.v.D.); 0000-0001-6164-1141 (R.M.); 0000-0002-5222-6648 (J.A.P.); 0000-0002-4463-2291 (J.B.); 0000-0003-0369-8777 (U.S.); 0000-0002-4086-2567 (S.J.).

Precise measurements of root system architecture traits are an important requirement for plant phenotyping. Most of the current methods for analyzing root growth require either artificial growing conditions (e.g. hydroponics), are severely restricted in the fraction of roots detectable (e.g. rhizotrons), or are destructive (e.g. soil coring). On the other hand, modalities such as magnetic resonance imaging (MRI) are noninvasive and allow high-quality three-dimensional imaging of roots in soil. Here, we present a plant root imaging and analysis pipeline using MRI together with an advanced image visualization and analysis software toolbox named NMRooting. Pots up to 117 mm in diameter and 800 mm in height can be measured with the 4.7 T MRI instrument used here. For 1.5 L pots (81 mm diameter, 300 mm high), a fully automated system was developed enabling measurement of up to 18 pots per day. The most important root traits that can be nondestructively monitored over time are root mass, length, diameter, tip number, and growth angles (in two-dimensional polar coordinates) and spatial distribution. Various validation measurements for these traits were performed, showing that roots down to a diameter range between 200 μm and 300 μm can be quantitatively measured. Root fresh weight correlates linearly with root mass determined by MRI. We demonstrate the capabilities of MRI and the dedicated imaging pipeline in experimental series performed on soil-grown maize (*Zea mays*) and barley (*Hordeum vulgare*) plants.

The root system is of critical importance for the survival, development, and performance of higher plants, because it is the major organ for anchorage, acquisition of water and nutrients, and carbon storage. Therefore, there is a long-standing interest in the scientific community regarding the structure, function, and development of root systems. Rising concerns about the environmental impact and increasing cost of fertilizers have initiated breeding programs for more resource-efficient cultivars and the development of methods for phenotyping root systems. The opaque nature of soils generally demands destructive methods such as root excavation for subsequent optical assessment (Lynch, 2007; Trachsel et al., 2011). Although efficient for screening large numbers of plants for a limited set of clearly discernible traits, this approach does not allow detailed monitoring of root development over time. Other approaches, such as rhizotrons or mini-rhizotron tubes, where root growth is observed along transparent windows (Nagel et al., 2009), monitor only a fraction of the roots. Methods in which the whole root system is visible are typically based on artificial media such as paper pouches (Chen et al., 2011; Le Marié et al., 2014), three-dimensional (3D) gels (Iyer-Pascuzzi et al., 2010), and hydro- or aeroponics (Herdel et al., 2001). Results may thus not be directly transferable to plants grown in natural 3D soil environments (Gregory et al., 2003). For example, roots are known to grow faster and thinner when the penetration resistance is low (Bengough et al., 2011; Chimungu et al., 2015). Computed tomography (CT; both x-ray and neutron) has been proposed to overcome the mentioned difficulties with studying roots in natural soil. CT has been successfully used to obtain high-resolution images of roots (Moradi et al., 2009; Flavel et al., 2012; Mooney et al., 2012). High resolution is necessary for segmenting roots due to a poor contrast between roots and soil (Jassogne et al., 2009; Mairhofer et al., 2012; Mairhofer et al., 2013). A first direct comparison (to our knowledge) of magnetic resonance imaging (MRI) and x-ray CT for 3D root imaging has recently been published (Metzner et al., 2015), showing that the two modalities pose different opportunities and limitations for root imaging.

MRI is based on the magnetic moment of atomic nuclei like ^{1}H (protons), which are highly abundant in living tissues, mainly in water molecules. The magnetic moment can be manipulated using strong magnetic and

[1] This work was supported in part by the Bundesministerium für Bildung und Forschung (BMBF) under grant no. 0315529/CROP. SENSe.net and in part within the German-Plant-Phenotyping Network under project identification no. 031A053, also funded by BMBF.

* Address correspondence to d.van.dusschoten@fz-juelich.de.

The author responsible for distribution of materials integral to the findings presented in this article in accordance with the policy described in the Instructions for Authors (www.plantphysiol.org) is: Dagmar van Dusschoten (d.van.dusschoten@fz-juelich.de).

J.K. and D.v.D. set up the MRI hardware and automated sample handling; D.P., D.v.D., J.A.P., and J.B. developed the data analysis toolbox; D.v.D., R.M., D.P., S.J., and U.S. designed the experiments, which were performed by D.v.D., R.M., and D.P.; and D.v.D., R.M., and S.J. performed the data analysis. All authors contributed to the preparation of the manuscript.

[OPEN] Articles can be viewed without a subscription.

www.plantphysiol.org/cgi/doi/10.1104/pp.15.01388

radio frequency fields that have no known impact on plant development to produce 3D datasets of samples. MRI offers several contrast parameters that can be manipulated for discriminating different structures such as roots from soil background (Rogers and Bottomley, 1987; Jahnke et al., 2009). The basic principles of MRI are described in detail in several textbooks (Callaghan, 1993; Haacke et al., 1999) or review articles (Köckenberger et al., 2004; Blümler et al., 2009; van As et al., 2009; Borisjuk et al., 2012). Research applications to plant roots range from phytopathology (Hillnhütter et al., 2012), across storage root internal structures (Metzner et al., 2014) and water uptake modeling (Stingaciu et al., 2013), to coregistration with positron emission tomography for investigating structure-function relations (Jahnke et al., 2009). Water mobility in roots and soil has also been shown to be detectable with MRI (MacFall and Johnson, 2012; Gruwel, 2014). In particular for imaging roots with MRI, these studies generally explored the applicability of MRI but largely lacked validation of the data against conventional techniques of root visualization after harvest. Our goal was to develop MRI protocols to image roots of plants growing in soil to obtain global root parameters such as root length, mass, or root diameters; gather root growth angles and number of root tips; get spatial information on the distribution of root system architecture (RSA) parameters such as root length densities; and, wherever possible, verify these parameters against harvest data.

RESULTS

Multiscale MRI

To demonstrate the performance of the MRI technique, different plant species in a variety of pot sizes were imaged (Fig. 1). For a maize plant (*Zea mays*; Fig. 1A), grown in a small pot with 51 mm i.d. filled with a mineral soil substrate, a small radiofrequency (RF) coil (64 mm i.d.) was used to get the magnetic resonance image shown in Figure 1B. The magnetic resonance images of both shoot and roots were acquired in four scans that were concatenated afterward, with each scan lasting 20 min and covering a block of 58 mm in the vertical direction. Plant structures, such as stem, leaves, roots, and residual seed, were clearly visible. The primary root (yellow asterisk in Fig. 1B) had spiraled down to the bottom and developed lateral roots along the way. Nodal roots were visible in the top section near the maize grain (white asterisk). Besides standard MRI data handling and performance of a noise cutoff, no further data processing was required to obtain the volumetric image. The finest roots that are visible in the image had estimated diameters of 150 μm to 200 μm, as found both by visual inspection of the roots after harvest and calculated from signal intensity (see Discussion).

A common bean plant (*Phaseolus vulgaris*) was grown in a container with 81 mm i.d. and 250 mm height (Fig. 1C). This required an RF coil with 100 mm i.d. resulting in 40% loss of signal compared to the smaller one used in Figure 1B. The signal loss was compensated by using a lower spatial resolution. These MRI data were acquired in three scans, each lasting 20 min and covering a block of 100 mm in height, concatenated afterward. Since MRI measures an integral signal, even roots with

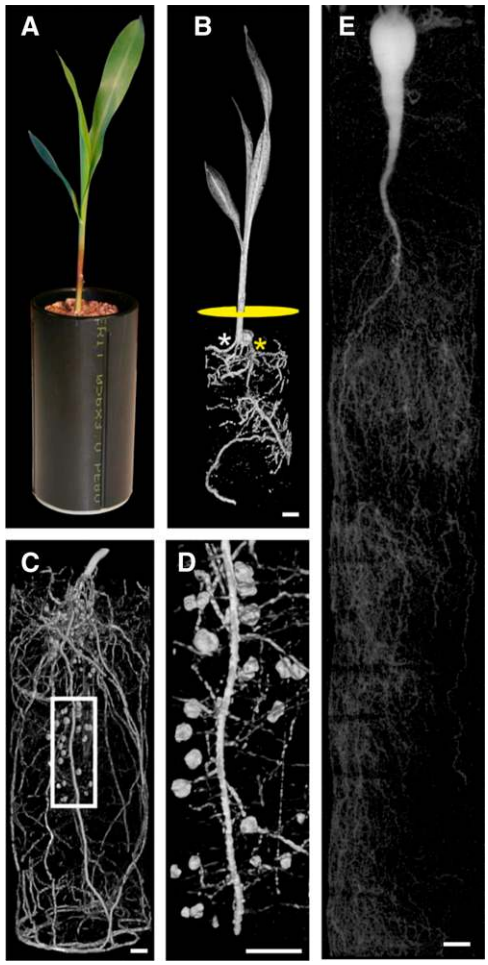

Figure 1. Images of a whole maize plant and root systems of a bean and a sugar beet plant. A, B, The maize plant was grown in a pot with 51 mm i.d. and 110 mm height. C, D, The bean plant was grown in a pot with 81 mm i.d. and 250 mm height and, E, the sugar beet plant was grown in a container with 117 mm i.d. and 800 mm height, all filled with a loamy sand mix. A, Digital photo of the maize plant taken 10 d after sowing (DAS) and, B, a rendering of a volumetric (3D) MRI dataset (T_E = 9 ms, resolution 0.33 × 0.33 × 0.8 mm^3) of the plant concatenated from four consecutively measured blocks along the vertical axis. The yellow disc denotes the soil surface in the magnetic resonance image for better orientation. The yellow asterisk denotes the primary root, the white asterisk a nodal root. C, Visualization of two concatenated magnetic resonance images (T_E = 9 ms, resolution 0.52 × 0.52 × 1.0 mm^3) of the root system of a bean plant (32 DAS) showing nodules at the top and central region. D, Zoomed image with nodules of various sizes and shapes attached to lateral roots (T_E = 9 ms, resolution 0.23 × 0.23 × 0.94 mm^3) depicted from the central root segment indicated in (C). E, Overview of the whole root system of a sugar beet plant (80 DAS) with the storage beet, the taproot, and a multitude of lateral roots. The image consists of six concatenated blocks with a resolution of 0.73 × 0.73 × 2 mm^3 (T_E = 9 ms). Scale bars: B, C, D, 10 mm; E, 20 mm.

diameters below the spatial image (i.e. voxel) resolution can be detected. The root signal is simply smeared out over the whole voxel and the location of these thin roots has therefore an uncertainty in the range of the voxel size. The finest roots that are visible in Figure 1C were estimated to be about 300 μm thick. In the image of Figure 1C, a multitude of roots, which grew shallow or down to the bottom of the pot and root nodules, could be identified. The zone with the highest density of nodules was scanned separately (Fig. 1D) using a higher resolution (data acquisition time, 35 min).

For larger plants with extended root systems, larger containers are required (Poorter et al., 2012). This also applies to below ground storage organs such as sugar beets (Metzner et al., 2014). Figure 1E shows a magnetic resonance image of an 80-d-old sugar beet (*Beta vulgaris*) grown in a container with 117mm i.d. and 800mm height (soil volume 8.6 L). The image has been constructed from six concatenated blocks, each 120 mm in height and taking 20 min to acquire, to show the entire root system including the storage beet at the top. Due to the size of the RF coil with 170 mm i.d., the spatial resolution was reduced in favor of a greater signal-to-noise ratio. Only roots with estimated diameters >450 μm were visible, albeit with obvious gaps. Despite the difficulty of detecting individual roots, the spatial distribution of roots in the pot was visible.

Noninvasive Root Trait Quantification

High quality 3D images of a root system can be used to extract quantitative trait parameters. A new program, called NMRooting, was developed for automated analysis of the MRI datasets (see "Materials and Methods"). We assessed our MRI method by comparing the data of 15-d-old maize and barley roots to data obtained after destructive harvest with the common methods of weighing, scanning, and analyzing with WinRHIZO software (Regent Instruments, Quebec City, Quebec, Canada).

When plotting the root fresh weight estimated by MRI against gravimetric measurements, linear regressions showed slopes of 0.69 (r^2 = 0.97) and 0.82 (r^2 = 0.64) for maize and barley, respectively (Fig. 2A), indicating that MRI on average detected 70% to 80% of the biomass. The fraction of detected root length was very similar and the slopes of 0.78 (r^2 = 0.63) and 0.81 (r^2 = 0.79) in Figure 2B for maize and barley, respectively, indicated a recovery rate of around 80% for both crops. Omitting all roots with diameters <200 μm from the WinRHIZO data and plotting the length against the total MRI root length gave slopes much closer to 1 (0.99 with r^2 = 0.94, and 0.91 with r^2 = 0.74 for maize and barley, respectively; Fig. 2C), while omitting all roots with diameters <300 μm, gave slopes above 1, i.e. 1.12 (r^2 = 0.96) and 1.14 (r^2 = 0.73) for maize and barley, respectively (data not shown). We compared the automated root detection procedure against a manual segmentation (see "Materials and Methods"). For young barley plants, both methods resulted in similar lengths

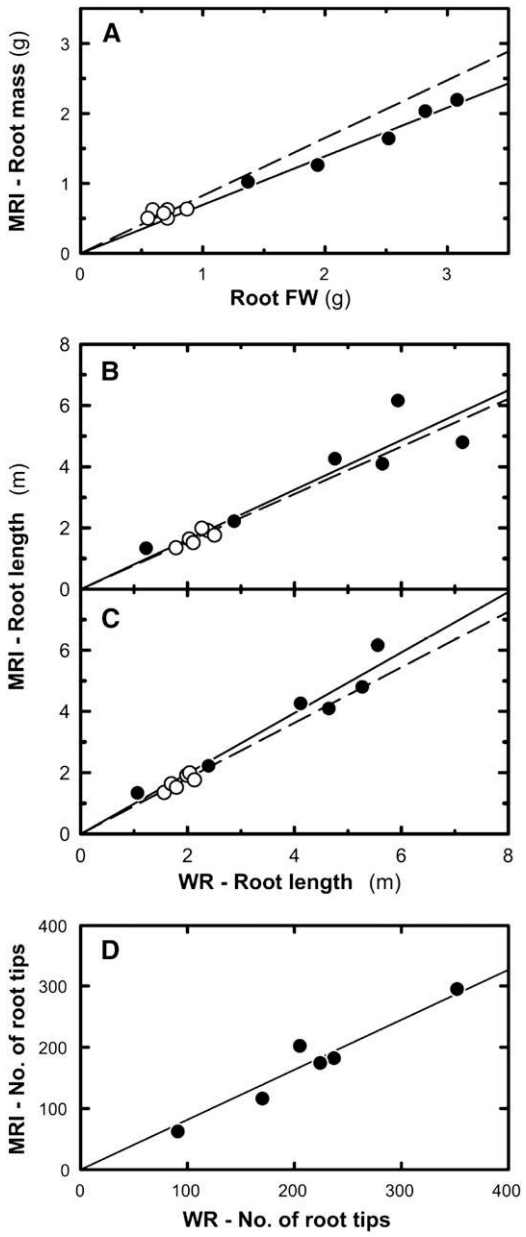

Figure 2. Different root traits obtained with MRI versus gravimetric or WinRHIZO measurements taken after harvest immediately after the end of the particular MRI experiment. Six maize (black circles) and six barley plants (white circles) were measured 15 DAS in pots with 81 mm i.d. and 300 mm height. A linear regression ($y = a^*x$) was fitted as a simple model (black and dashed lines for maize and barley, respectively). A, Root mass measured with MRI is displayed versus gravimetrically measured root FW, resulting in a slope of 0.69 for maize and 0.82 for barley. B, MRI root length versus WinRHIZO root length where all roots monitored with WR were taken, resulting in slopes of 0.81 for maize and 0.78 for barley. C, The same data as in (B), but here only roots with diameters >200 μm were considered for the WinRHIZO data resulting in slopes of 0.99 for maize and 0.91 for barley. D, Number of root tips detected with MRI versus WinRHIZO for maize roots with diameters >300 μm showing a slope of 0.82. FW, fresh weight; WR, WinRHIZO.

(Supplemental Fig. S1) while, for older and longer root systems, the automated routine detected more root lengths compared to the manual routine. This additional root length can be attributed to emerging lateral roots that were detected by the automated routine but overlooked by manual analysis as these small roots were close to the noise threshold. A few of the automatically detected laterals were false positives.

We also determined the number of root tips and growth angles of seminal roots. Compared to WinRHIZO, MRI detected on average 82% of the maize root tips of roots thicker than 300 μm (Fig. 2D). Due to the simplicity of the barley root system at seedling stage, for this species it was also possible to calculate the initial root angle of the seminal roots using the NMRooting program returning a mean branching angle of 54.6° ± 15.2° (SD, n = 34 individual seminal roots of six barley plants) relative to horizontal (data not shown). For maize plants, the multitude of roots in the top part of the pot did not allow for an automated extraction of root angles for specific root types; however, a method to extract mean root angles also for complex root systems is described later on (compare with Fig. 6).

Root diameters of a maize plant were estimated with NMRooting just before harvest and superimposed in false color on the grayscale MRI data (Fig. 3A). The shoot and the seed had the largest diameters and were by this criteria excluded from the analysis. The primary root could be followed to the bottom and had an average diameter of 1.3 mm. The seminal roots originating from the embryonic scutellar node (Hochholdinger, 2009) had slightly smaller diameters (all in yellow) while crown roots had diameters well above 1 mm. Most lateral roots had diameters of around 0.5 mm or less. Some gray pixels can be recognized (e.g. in the lower-third of the image) that were not connected to the root system as they did not meet the criteria used for automatic root system extraction and might have represented local pockets of soil water. Determination of root diameters allowed us to split the root length over 100 μm diameter classes, as is commonly done with WinRHIZO. We plotted these root length data by diameter class for four maize (Fig. 3B) and six barley (Fig. 3C) plants, which shows that MRI revealed similar lengths for all diameter classes except for those <300 μm. The overestimation of root length in the diameter class 400 μm to 500 μm by MRI for maize (Fig. 3B) might be caused by a systematic error in the diameter estimation (either by the NMRooting or the WinRHIZO program), which would shift roots from one diameter class into another. Regressing the lengths measured for both methods for each and all root diameter classes, we found slopes of 0.89 (r^2 = 0.66) and 0.81 (r^2 = 0.68) for maize and barley, respectively (Supplemental Fig. S2). When all roots with diameters <300 μm were omitted from the WinRHIZO data, the slopes of the linear regressions (displayed as solid lines in Supplemental Fig. S2, A and B) were not significantly different from 1 for either maize or barley roots (0.99 with r^2 = 0.75 for maize, and 1.04 with r^2 = 0.92 for barley roots).

Quantification of Root Growth

To assess the dynamics of root growth, the maize and barley plants presented in the previous section were repeatedly measured with MRI during the two weeks prior to harvest. A time series of measurements for one maize plant on 6, 9, 12, and 15 d after sowing (DAS) is depicted in Fig. 4. Figure 4, A–D, shows a two-dimensional (2D) maximum intensity projection (MIP) of the 3D MRI data. Some signal arising from soil water can be seen at the bottom and some small spots of water were scattered throughout the pot (Fig. 4). These spots, however, are few in number and quite isolated in 3D

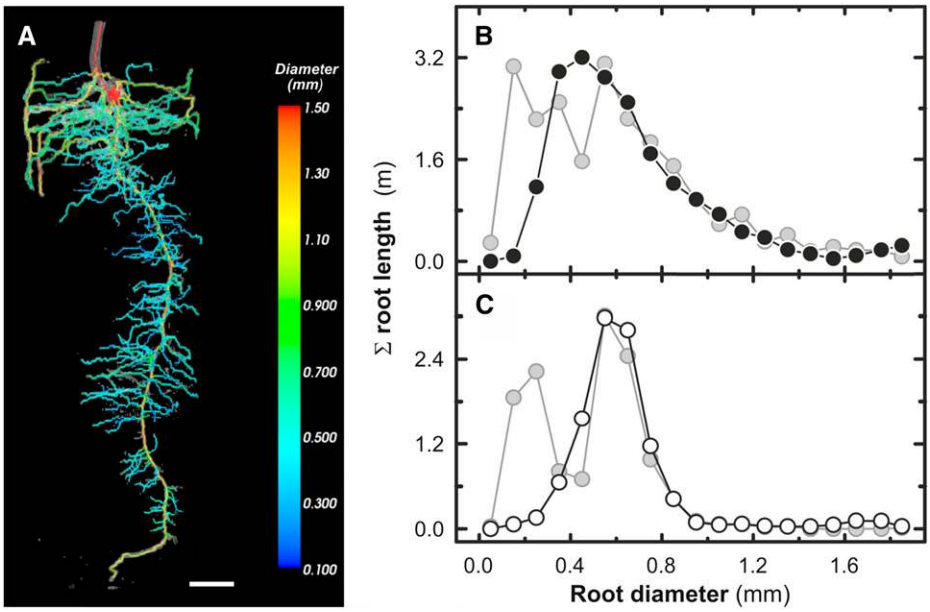

Figure 3. Comparison of root diameters of maize and barley plants obtained with MRI versus WinRHIZO. A, Magnetic resonance image of a maize root system (15 DAS) coregistered with a diameter estimation of each root segment based on the local MRI intensity and drawn in false colors. The sum of all root lengths per root diameter class as determined by MRI (black or white circles) or WinRHIZO (gray circles) is shown in (B) of four maize plants and in (C) of six barley plants at 15 DAS, respectively. Pot size, see Figure 2, scale bar = 20 mm.

space. In Figure 4B, a small nonattached root seems to appear lower down the column, which was identified as a germinating weed that later died, upon which the MRI signal also vanished (see Fig. 4D). The maize seed gained in signal intensity during this early growth period. In Figure 4A, two seminal roots are visible just below the seed when the primary root was already well established. A few nodal roots had started to grow by DAS 9 (Fig. 4B), likewise a large number of lateral and nodal roots that encountered the boundary of the pot bending downward by DAS 12 (Fig. 4C). Lateral roots had overall lower signal intensity than other roots because they were thinner than the voxel size, i.e. the signal of such voxels is then a mixture of root and (vanishingly low) soil signal. The growth of laterals was not homogeneous along the primary root; for example, most laterals in the lower-half of the pot were longer than those in the upper-half (Fig. 4D). For obtaining a better 3D impression in which individual roots are easier to recognize, a 3D surface rendering of the same data set is given in Figure 4, E–H. Here, the first step for the automatic trait extraction has already been applied to the data, i.e. all residual MRI signals more than 3.5 mm apart from the root system were deleted. In this surface rendering, however, the signal intensity information is lost, leading to an over-emphasis of the thickness of lateral roots. In Figure 4, G and H, it can be easily seen that the nodal roots grew downward after reaching the pot surface, while lateral roots tended to follow the pot curvature. The signal of lateral roots is sometimes discontinuous due to small local disturbances in the magnetic field, but this does not mean that these roots were not attached to the plant. These small (<3.5 mm) gaps were closed in the extraction of the 3D morphological skeleton of the roots using NMRooting and added, on average of all root systems analyzed here, less than 5% to the total root length.

Figure 4 shows images of only four days of an experimental series where MRI data were acquired at six different days (6, 9, 10, 12, 13, and 15 DAS) for which root length, MRI root mass, and the number of root tips (the latter only for maize) were calculated (Fig. 5). During DAS 6–15, the development of the three root traits appeared to be close to linear. The mean root growth rate was calculated to be 0.51 m d^{-1} for maize and 0.13 m d^{-1} for barley (Fig. 5A) and the root mass increased by 0.13 g d^{-1} for maize and 0.035 g d^{-1} for barley (Fig. 5B). The number of root tips was analyzed for maize only and increased with 21.7 d^{-1} (Fig. 5C). The average diameter of the maize roots decreased from 1.25 mm (SD = 0.06) at 6 DAS to 0.67 mm (SD = 0.06) at 15 DAS (data not shown; for calculation, see "Materials and Methods") as an increasing proportion of root length was formed by lateral roots (compare with Supplemental Fig. S3A). The average root diameter of barley did not change significantly during this early growth stage, but fluctuated around 0.62 mm (SD = 0.056), since at this stage hardly any laterals were visible (Supplemental Fig. S3B). In one out of the 60 measurements presented in Figure 5, excessive soil

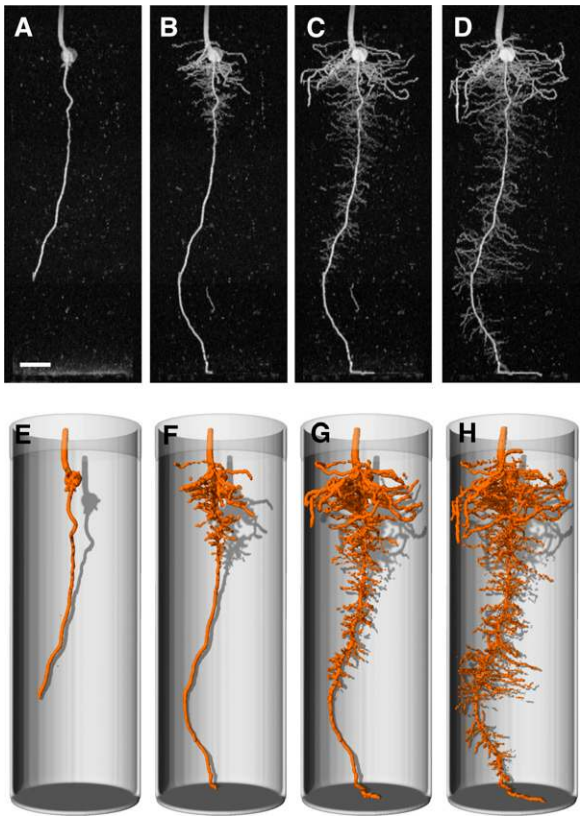

Figure 4. Root growth of a maize plant in soil monitored over several days with MRI. A, B, C, D, MRI data acquired at four different growth stages (6, 9, 12, and 15 DAS) are displayed as 2D maximum intensity projections (MIPs). E, F, G, H, shows the same data set as 3D surface renderings with a virtual illumination from the top casting a shadow on the inside of the digitally added pot. For clarity, residual MRI signals that were more than 3.5 mm apart from the root system have been removed in the 3D rendering. Pot size, see Figure 2. Scale bar = 20 mm.

water led to an overestimation of the root traits. A manual correction of the automatically extracted RSA could mitigate this effect. This feature, however, is not implemented in the NMRooting software used here.

Analysis of Spatial Root Distribution

The RSA of grown root systems is often described by a limited set of aggregate traits like root length or root mass. The spatial distribution of these variables is often ignored, even though it may contain valuable information related to soil heterogeneity. However, due to stochastic variation, the precise 3D location of individual roots as acquired by MRI is not informative by itself and difficult to present on paper. So far, we presented 2D projections (Fig. 1, Fig. 3, and Fig. 4), reducing the dimensionality of the data by aggregating along a horizontal axis. A dimensional reduction can also be achieved by assuming that plant root systems have cylindrical symmetry (Fig. 6). The MRI signal of one young barley plant (13 DAS) was integrated along a

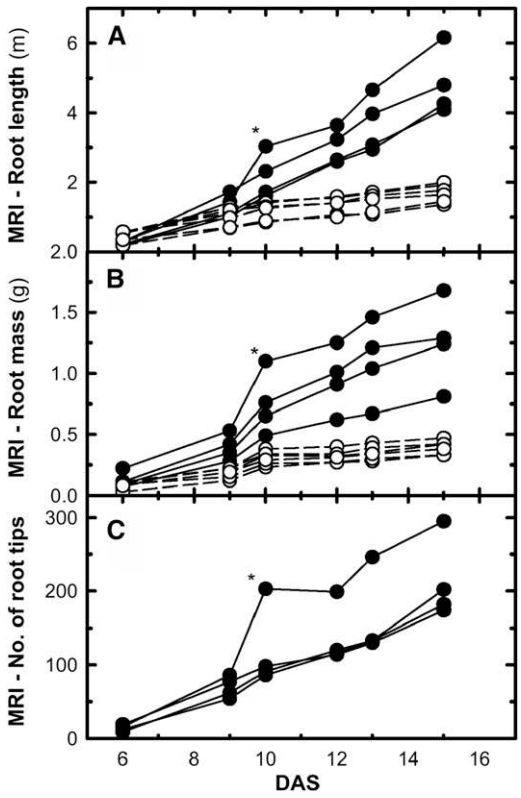

Figure 5. Development of different root traits of maize and barley plants monitored over time with MRI. Pot size was 81 mm i.d. and 300 mm height for all plants. The MRI measurements were routinely performed between 6 and 15 DAS. The development of four maize plants (black circles, solid lines) and six barley plants (white circles, dashed lines) are shown. In the measurement marked by the asterisk, excessive soil water at the pot bottom led to a residual MRI signal from the soil water. This resulted in an overestimation of the respective root traits by the automatic data extraction. A, Length of roots; B, root mass; C, number of root tips (for maize only).

circle for each distance to the center (r) at each depth (z), as denoted in Figure 6A, resulting in the angular projection shown in Figure 6B. For a more complex root system at a later stage (38 DAS), both the 2D MIP image and the corresponding angular projection are shown in Figure 6, C and D, respectively. To present the spatial distribution of root traits, the data is depicted as 2D heat maps in Figure 6, E, G, J, L, and N. These maps present averages (n = 5 barley plants) of root mass density (Fig. 6E), root length density (Fig. 6G), root tip density (Fig. 6J), mean root angle (Fig. 6L), and mean root diameter (Fig. 6N). In root biology, one-dimensional (1D) depth profiles are commonly presented and therefore we further reduced our 3D MRI data to 1D vertical profiles for root mass (Fig. 6F), root length (Fig. 6H), number of tips (Fig. 6K), root angle (Fig. 6M), and root diameter (Fig. 6O). The angular projection maps of root mass densities, root length densities, and root tip densities showed similar distribution patterns for these traits (Fig. 6, E, G, and J, respectively). In addition, the depth distribution of root mass, root length, and number of root tips matched also rather well (Fig. 6, F, H, and K, respectively). Figure 6, L, M, N, and O, shows that the 2D distribution maps contain more information than the 1D depth profiles, as the mean values of root angles or root diameters (Fig. 6, M and O, respectively) were rather similar along the vertical axis but not at radial distances from the shoot (Fig. 6, L and N, respectively).

DISCUSSION

We demonstrated a versatile 3D technique for noninvasive imaging of roots growing in soil (Fig. 1). The technique is based on a vertically placed MRI instrument, a slightly adapted soil, and optimized measurement protocols. We developed a data analysis tool that computes root traits from the acquired images including root mass, lengths, diameters, angles, and number of root tips. Our results were in good agreement with those obtained by gravimetric and WinRHIZO measurements (Fig. 2 and Fig. 3) and we conclude that, in future root studies, MRI can be used to gather such information nondestructively on a routine basis.

The MRI signal that we measure comes from protons (^{1}H) of, mostly, water. We distinguish between water in the root and water in the soil that, based on the soil composition, water content, and magnetic field strength, can cause the signal of soil water to decay much faster than that of root water. This effect has been noticed and exploited by other authors (e.g. Brown et al., (1991), but was not explained in detail. The decay of the soil water signal in our system is so fast that our images contain virtually only signals of roots and thus have good contrast to the soil. This contrast (see e.g. Fig. 1) allows for simple image segmentation using only a noise cutoff. The MRI signal of root water, after signal decay correction and calibration, is proportional to the water amount and, by that, a measure of root fresh weight. Plotting the root mass detected by MRI against the gravimetrically determined fresh weight gave a good, linear correlation (Fig. 2A). This suggests that MRI detected 70% to 80% of root mass. However, as discussed below, MRI detects about 80% of the total root length, and the remaining 20% was most likely comprised of roots with diameters $<$200 μm, which contribute little to the total root mass (relative to their length). Therefore, it may be questioned whether the suggested underestimation of root mass by MRI is not a result of overestimation of the mass determined gravimetrically. This could easily happen if water, or soil, adheres to roots after washing, a common problem in fresh weight determination (Bashan and de-Bashan, 2005). It is difficult to assess this, because other sources of error such as, for example, the T_2 correction or calibration (see explanation and discussion further down), are also possible. We conclude that MRI, as used here, detects at least 70% of the root mass for maize and barley.

By tracing roots with NMRooting we detected about 80% of the total root length found with WinRHIZO (Fig. 2B). To evaluate which root fraction was not captured

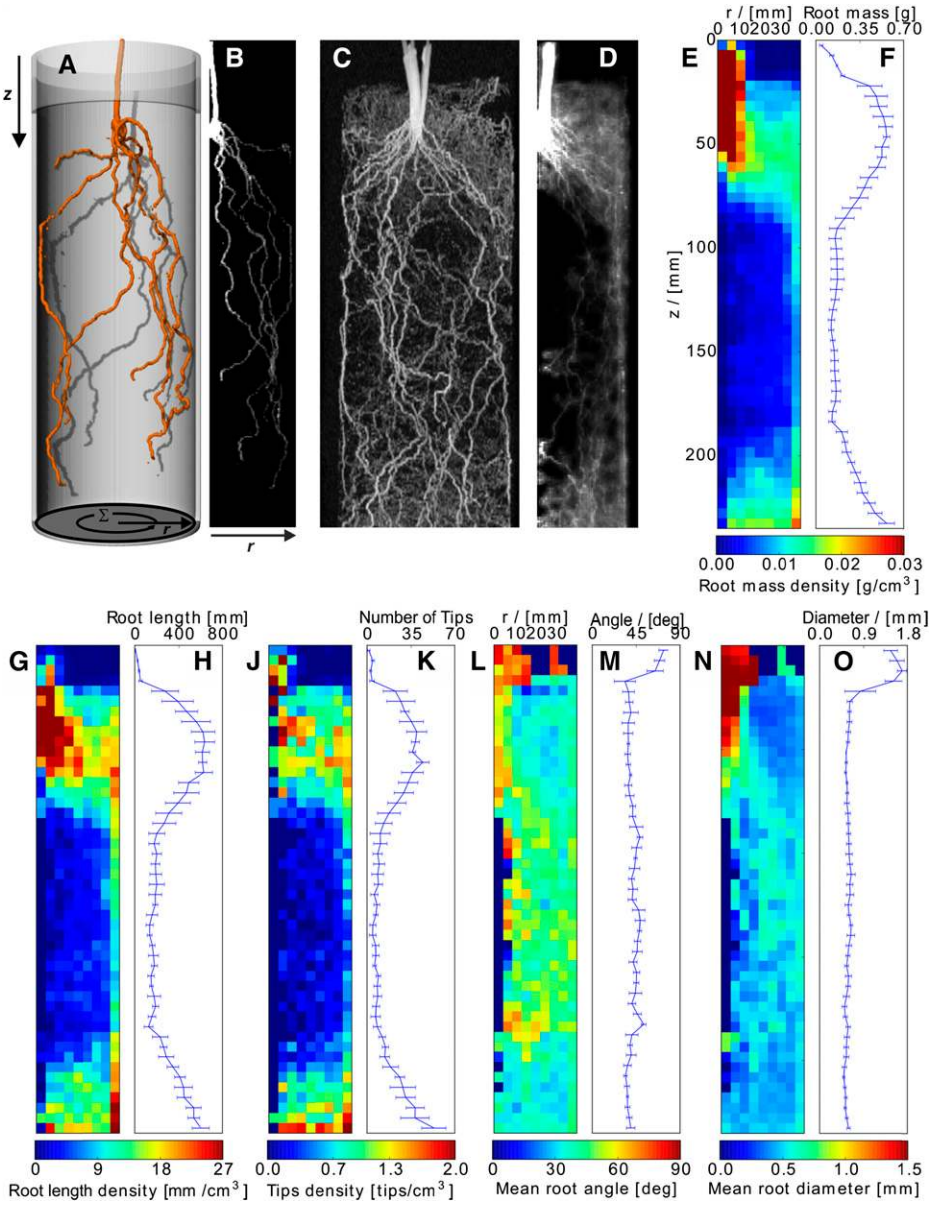

Figure 6. Magnetic resonance images and projections illustrating the spatial distribution of different root traits in 2D panels. A, Magnetic resonance image with shadow effects illustrating the 3D structure of the root system of a barley plant (13 DAS). The scheme at the bottom illustrates how an angular projection was performed. B, The resulting 2D image obtained after angular projection of (A). C, A standard MIP image of an older barley root system (38 DAS). At this stage of development, the spatial distribution of the roots is hard to grasp and (D) shows the angular projection of the root system visualizing the radial distribution of the roots. E, F, G, H, I, J, K, L, M, N, O, The 2D radial distribution (E, G, J, L, N) and 1D depth distribution (F, H, K, M, O) of values of various root traits are presented for five barley plants grown in pots with 81 mm i.d. and 300 mm height and measured at 38 DAS. E, G, J, L, N, Mean values (n = 5) of the radial distribution of different traits for which the data were binned to 5 × 5 mm^2. F, H, K, M, O, Mean values ± SD (n = 5) of depth distribution of the traits is shown for which the data were binned to 5 mm slices in the vertical direction. E, F, Root mass density; G, H, root length density; J, K, Root tip density; L, M, mean root angle relative to soil surface; and N, O, mean root diameter.

by MRI, we estimated root diameters from MRI signal intensity, plotted the root length by diameter distribution, and compared with WinRHIZO data (Fig. 3). MRI root length was almost identical to WinRHIZO data for roots >200 μm diameter but MRI obviously failed to detect roots <200 μm (Fig. 2C). The loss of thinner roots, supposedly mainly fine laterals, can be explained by NMR physics, as discussed further down. This threshold, however, is not a fixed value but depends on many factors, including the used soil or hardware and may thus differ for different setups. For example, for smaller pots (e.g. with 51 mm i.d.), we used a 64 mm RF coil and estimated that we could thereby detect roots as thin as 150 μm to 200 μm (Fig. 1B). As MRI, root analysis with x-ray CT also acquires, with current root segmentation procedures, similar fractions of roots compared to WinRHIZO (Flavel et al., 2012; Metzner et al., 2015). Koebernick et al. (2014) reported a detection of near 100% for roots of *Vicia faba* regarding only roots >500 μm. Many x-ray CT studies unfortunately do not report verification of detected root traits by comparison with harvest data. So far, all existing methods for measuring soil-grown roots only sample a part of the root system. Even WinRHIZO data may include significant errors from root washing (Amato and Pardo, 1994) or scanning procedures (Himmelbauer et al., 2004), and may be biased against fine roots (Zobel, 2008). Nevertheless, we used WinRHIZO as a reference as it is one of the most commonly used methods for determining plant root traits. The missing root fraction in the MRI data is relatively well defined, and thus poses no problem for data interpretation.

Root diameters have been found to depend on soil strength (Kirby and Bengough, 2002), soil water content (Kuchenbuch et al., 2006), or nutrition levels (Zobel et al., 2007), and thus the ability to accurately determine diameters may be of importance for many studies. It is difficult to say what the precise accuracy is of our diameter estimates, as we do not have a coregistration of the magnetic resonance images with the WinRHIZO scans. However, visual comparison of WinRHIZO selected roots with the diameter by root length estimations (Fig. 3) suggests that diameters can be determined with sufficient accuracy.

Root branching angles and the gravitropic response of the major root axes are known to greatly influence shallow versus deep rooting. Shallow rooting has been proposed to increase phosphorus uptake efficiency, while deep rooting have been proposed as beneficial for nitrate and water uptake (Wasson et al., 2012; Lynch, 2013; Trachsel et al., 2013). However, accurate determination of angles is often possible only in 2D systems or, after excavation, for relatively stiff roots (Trachsel et al., 2010; Colombi et al., 2015). Our NMRooting approach calculated branching angles of every root of a single plant in 3D (for details, see "Materials and Methods"). For example, barley seminal roots had a mean initial branching angle of 54.6° from horizontal. Determining gravitropic responses is theoretically possible but, despite the relative large pot sizes, the growth directions of many roots were obstructed in the experiments performed here (e.g. Fig. 4).

The lateral branching density may vary strongly among genotypes or with local soil conditions and is proposed to be an important factor for nitrate and phosphorus acquisition (Postma et al., 2014). Our detection of the number of tips, however, is sensitive to the image segmentation parameters while the number of tips in WinRHIZO data is easily influenced by the breaking of roots. Nevertheless, the data for maize (Fig. 5) suggests that about 80% of the root tips belonging to roots >300 μm in diameter were detected here with MRI and that, from it, careful estimates of lateral branching density may be possible.

MRI can be also used to investigate the distribution of special structures such as nodules in legume species such as bean (Fig. 1, C and D). The size and anatomy of below-ground storage organs as, for example, sugar beet (Fig. 1) can also be addressed and the application of this was already described (Metzner et al., 2014; Schmittgen et al., 2015). However, relatively little is known about the root system of the sugar beet plant below the storage organ, and the demonstration that MRI is applicable even for large pots (compare with Fig. 1E) may raise interest for further investigations in this field.

With MRI, root traits can be acquired without destructive harvest or root washing that reduces labor and retains the original 3D structure of a root system in soil. The 3D distribution of roots is thought to be of importance as resources are not homogeneously distributed in the soil. The precise positioning of roots, however, contains a significant amount of stochasticity that is not easily explained and may be part of a bet-hedging strategy (Forde, 2009). Some form of spatial aggregation and/or dimensional reduction is thus necessary in order to compare plants. 1D depth profiles are often presented in the literature. Figure 6 shows a quasi 3D representation, 2D angular projections, and 1D depth profiles of the same data. We regard the angular projections as particularly useful as plants typically have an almost round shape in the horizontal plane. The angular projections show branching angles from the middle of the plant outwards and, in Figure 6, E, G, and J, the root densities in the middle of the pot were relatively low compared to those near the pot wall. Exceptions are seen near the shoot and close to the bottom of the pot. Since Figure 6, E, G, and J, display densities the data were corrected for the variable volume across integration was performed. On the other hand, Figure 6, L and N, display mean root characteristics (diameters and angles) that are independent of the amount of roots. For example, Figure 6N shows lower mean root diameters near the top and bottom of the column, which correspond to greater placement of lateral roots in those parts of the pot. The density of root tips (Fig. 6J) seems to correlate well with the root length density (Fig. 6G). Theoretically, plants should place their root tips close to relatively unexplored soil domains as to not have newly grown roots compete with existing ones. Here, the plants did clearly not distribute their roots throughout the pot evenly which, in part, may be a limitation of pot studies (Poorter et al., 2012). We conclude that the 3D information in the magnetic resonance images allows for the determination of important root architectural traits and that angular projection may show the spatial information better than the more common profiles in Cartesian coordinates.

Additionally, we could monitor the development of the root system in soil over time (Fig. 4 and Fig. 5). Currently, detailed 3D growth analysis of roots requires artificial hydroponics or gel systems or destructive harvests needing a large number of plants to be measured. When time series are depicted from the latter approach, they may contain much variation coming from the plant-to-plant variation. Noninvasive measurements are thus a great advantage over destructive measurements. In principle, the growth rates of both a whole root system and individual roots can be determined by comparing magnetic resonance images of the same plant. Figure 5 shows example results of the root length development of maize and barley plants over 9 d with clearly higher growth rates of the larger seeded maize plants; the error bars for maize were greater than that for barley and can be explained by plant-to-plant variation. With MRI it is possible to monitor growth over even a much longer time (e.g. 3 months) as already shown for the development of sugar beets (Metzner et al., 2014), which is a great strength of MRI.

Acquisition of Magnetic Resonance Images

Acquisition of magnetic resonance images and the good contrast between soil and root water is based on

the fact that signal decay of water in our soil and at 4.7 T is much faster than that of the water in the root (relaxation time $T_{2,soil} << T_{2,root}$). Typical values measured for the relaxation times are $T_{2,soil}$ <3 ms and $T_{2,roots}$ approximately 20 ms to 40 ms. Thus by adjusting the echo time (T_E) to 9 ms after giving a pulse, we can obtain an image of the water in roots, without receiving signals of soil water (repetition time, T_R, was set to 2.85 s). Mathematically, the MRI signal can be presented in simplified form as

$$S = K \times \left[V_{root} \times \exp\left(-T_E/T_{2,root}\right) + V_{soil} \times \exp\left(-T_E/T_{2,soil}\right)\right] + \sigma \quad (1)$$

where S denotes the measureable NMR signal from a volume (a voxel); K equals the calibration constant of the MRI equipment and the used protocol; T_E denotes the echo time of the experiment; $T_{2,root}$ and $T_{2,soil}$ represent the relaxation times T_2 of root and soil water, respectively; σ denotes the signal noise; and V equals the water volume. Here we assume a constant water density of 1 g cm^{-3}, thus the water volume is directly proportional to the amount of water in a voxel.

When the calibration constant K is also known, the volume of a subvoxel root element can be calculated based on the measured signal. For a given noise cut-off value, this can be used to estimate the minimal root diameter still detectable with our protocol. We determined K using the measured signal value of a water-filled voxel. With the assumption that $T_{2,water} >> T_E$ and the measured signal value of S_{water} = 4.0 a.u., we obtained from Eq. 1 $K = S_{water}/V_{Voxel}$ = 4.0 a.u./(0.5 × 0.5 × 1.0 mm^3) = 16 a.u. mm^{-3}. To generate a signal above threshold, Eq. 1 shows that the root water volume must be at least $V_{root} = \frac{S_{cutoff}}{Ke^{-T_E/T_2}}$. Assuming that a root consists of 90% water, the minimal root diameter still detectable from a cylindrical root is thus given by $d = \sqrt{\frac{4S_{cutoff}}{0.9\pi hKe^{-T_E/T_2}}}$. With the used noise cutoff of S_{cutoff} = 0.18 a.u., the voxel size of h = 0.5 mm, and the echo time of T_E = 9 ms, we obtained as minimal detectable root diameter d = 0.20 mm for roots with T_2 = 40 ms, and d = 0.22 mm for roots with T_2 = 20 ms, which is in good accordance with the experimental findings showing a root detection limit between 200 μm and 300 μm.

The enhanced decay of the NMR signal of soil water compared to root water is caused by local distortions (ΔB_z) of the magnetic field due to different magnetic susceptibilities (χ) of air, water, and soil particles. For a spherical soil particle of radius (R) submerged in water, these distortions to the main magnetic field (B_0) can be calculated using polar coordinates (r, Θ) according to (Schenck, 1996)

$$\Delta B_z(r,\Theta) = \frac{(\chi_{soil} - \chi_{water})}{3} B_0 \left(\frac{R}{r}\right)^3 \left(3\cos\Theta^2 - 1\right) \quad (2)$$

The enhanced MRI signal decay results from the diffusion of water molecules along the field distortions and is dependent on the gradient of Eq. 2 (Callaghan, 1993). The factor $\left(\frac{R}{r}\right)^3$ in Eq. 2 shows that small soil particles cause fast but local signal decay, while large particles result in slower decay over a wider range. Small-scale disturbances cause the soil water not to be visible in our images and are desirable for increasing contrast whereas larger-scale disturbances would also affect the water in the root and thus reduce the contrast in the images.

Furthermore, Eq. 2 states that the signal decay is dependent on the susceptibility difference χ_{soil}-χ_{water}. Typical values of χ are 0 for vacuum, -9.05×10^{-6} for water, -16.3×10^{-6} for SiO_2, and 2×10^5 for iron (Schenck, 1996; all values and Eq. 2 in the SI unit system). Components that may be particularly considered for small-scale distortions in the magnetic field are in the order of declining impact on MRI signal: (1) ferromagnetic particles (FMPs), (2) paramagnetic particles, (3) paramagnetic ions in solution, and (4) surface wall relaxation. FMPs have such strong effects that they need to be removed from the soil performed here by a protocol described in "Materials and Methods". Paramagnetic ions like Fe(II), Mn(II), or Ni(III) affect MRI signals to a much lesser extent (Box, 1996; Asseng et al., 2000) and the magnitude of the effect depends on the measurement parameters not further discussed here. Under controlled conditions, accumulation of Mn^{2+}, a very strong paramagnetic ion, in the roots should remain low (<100 μM; Vlamis and Williams, 1970), which is below the concentration (approximately 300 μM) where MRI signal intensity, given our protocols, would be seriously affected. In manganese-rich soils, Mn^{2+} accumulation may cause an enhanced signal decay. More relevant for achieving good magnetic resonance images are paramagnetic soil particles, primarily those containing Fe(II)O and Fe_2(III)O_3. Water close to these particles loses all signal intensity while water inside roots, which is spatially further away, remains mostly unaffected. For fine roots, a large fraction of the root water is in close proximity to soil particles, which can lead to a reduced relaxation time T_2 leading to a higher root detection limit, as detailed above. Surface wall relaxation, caused by e.g. paramagnetic ions on the soil particle surfaces, plays a minor role since it will be dominated by susceptibility effects when the condition $\Delta\chi \times B_0 << 10^{-5}$ T is not met (Mitchell et al., 2010), as is the case here.

As soil properties influence the MRI signal, it is possible that better root images can be obtained using different soil types or mixtures. For example, Brown et al. (1991) obtained good magnetic resonance images of conifer roots using a mixture of quartz sand, peat moss, and kaolinite clay. Here we used a mixture of coarse quartz sand and sandy loam taken from an agricultural field (see "Materials and Methods"). Coarse quartz sand (nearly pure SiO_2) has little influence on the MRI signal while especially silt particles improve the contrast between soil and root.

Analysis of Magnetic Resonance Images

In order to ease the analysis of complex 3D datasets obtained with MRI, we developed NMRooting, software

for segmenting roots in magnetic resonance images and determining different traits as discussed above. The segmentation may have introduced minor errors and some of the results, like the number of root tips, are sensitive to the segmentation parameters (data not shown). This may mean that, although the average detection is rather good (e.g. Fig. 2), the aggregate numbers may hide certain errors as they average out. As we lack a perfect ground truth for individual root segments, we can only estimate and discuss potential sources of errors: (1) Converting raster data to vector data introduces numerical errors, which overestimate the root length (see e.g. Dorst and Smeulders, 1987). Smoothing the root model could mitigate this effect, but may also remove true perturbations in the root growth trajectory. (2) Nonroot artifacts, such as water pockets or weeds, may be added to the root length when they are in the vicinity of a root. This, however, can easily be amended by manual correction. (3) Short lateral roots (<5 mm) are automatically removed, considerably shortening the total root length and reducing the number of root tips. This effect is most evident for thin roots that have a lower average length compared to thicker roots. Many of these detected short laterals are not true roots but false positives as they simply connect neighboring pixels in thicker roots or adjacent pixels that, due to soil water or noise, happen to have a signal intensity just above the noise cutoff. (4) Roots that can still be recognized by eye were sometimes not detected by the NMRooting program, mostly because of gaps larger than 3.5 mm (defined here as a threshold for automated gap filling), presumably caused by FMPs or paramagnetic particles that were still present in the soil. Based on the good correlation between MRI and WinRHIZO data (Fig. 2 and Fig. 3), the above-mentioned factors are assumed to roughly cancel out each other. A comparison with a manual root length determination procedure that looked only at the seminal roots of six barley plants also suggests that automated segmentation on average is close to the manual segmentation (Supplemental Fig. S1). We judge that magnetic resonance image segmentation may be improved as new algorithms are being developed and image quality increases.

CONCLUSION

Here we demonstrate that MRI can be used for noninvasive imaging of roots grown in relatively large (up to 8.6 L) soil-filled pots. The technology allows determination of important root traits such as length, mass, growth angles, diameters, or number of tips and their respective 3D distribution within a soil column. Most of the root mass of barley and maize roots were detected by the MRI approach as described above, and nearly all of the root length of the roots was thicker than 200 μm. The noninvasive nature of the modality makes it possible to monitor the development of root system architecture of individual plants over time and thereby to investigate root growth rates in soil. This provides unprecedented possibilities to study dynamic effects of stress or changing environmental conditions on live root systems. Automation enabled us to measure 18 plants per day. There is still potential to optimize the protocols and image segmentation procedures, so we expect that the root detection limit can be further decreased. This would make MRI measurements applicable also for plants with even finer root systems than those of the maize and barley plants investigated here.

MATERIALS AND METHODS

Soil Substrate

Sandy loam soil was taken from an agricultural field (A horizon, 0-30cm depth) near Kaldenkirchen, Germany with 73% sand (mostly fine), 23% silt (mostly coarse), 4% clay (Pohlmeier et al., 2009), and a low fraction (<0.2% w/w) of ferromagnetic particles (FMPs). After drying, the soil was homogenized with a Drum hoop mixer (J. Engelsmann, Ludwigshafen, Germany) and sieved to 2 mm. Stronger FMPs were removed by passing the soil on a conveyor belt through a magnetic field provided by rare earth magnets (NdFeB with a size of $9 \times 4 \times 1$ cm^3 and a remanence of 1.5 T (MCE, Bedfordshire, UK). Coarse quartz sand (grain size 0.7–1.4 mm; Quartzwerke Witterschlick, Alfter, Germany) similarly processed by using a shaker table to remove most FMPs was then mixed with the soil (2:1, v/v). The coarse sand was used to improve soil aeration that was otherwise poor in the sandy loam, as the soil processing destroyed the larger soil aggregates. The resulting mix was filled into PVC tubes of various sizes depending on the plant species and duration of the study. The tubes were fitted with a perforated bottom for water drainage and aeration with the holes covered by nylon mesh (grid size = 200 μm). The water holding capacity for this loamy sand mix was 18±2% v/v for the containers that were shorter than 400 mm, and the wilting point laid at around 3% water content. The bulk density of the mix varied between 1.6 and 1.75 kg/L. The soil strength was 40 kPa at full water holding capacity, increasing to 500 kPa when dried as measured using a penetrometer (Eijkelkamp, Giesbeek, The Netherlands). This is sufficiently low for good root growth (Kirby and Bengough, 2002) even at the relatively high bulk densities.

Plant Cultivation

Seeds of sugar beet (*Beta vulgaris* L. var Pauletta), barley (*Hordeum vulgare* L. var Barke), and maize (*Zea mays* L. var Badische Gelbe) were planted directly into the substrate. Watering was provided by automatic drip irrigation with nutrient solution. Depending on age and plant size, 15–60 mL Hakaphos blue solution (Compo, Münster, Germany) per day was given, increasing in concentration from 1 to 5% of the stock solution over time. Stock solution was prepared according to manufacturer's instructions with concentrations of N 1 M, P 0.14 M, and K 0.32 M. Irrigation was withheld at least 8 h prior to MRI measurements, allowing for sufficient water drainage and minimizing water loss (<5 mL per night). MRI measurements were performed when the soil water content was in a range of 12–15% v/v. Plants were grown in a climate chamber in a 16-/8-h light/dark regime, 20°C during light, 16°C during darkness, and constant relative humidity 60%. Lighting was provided by 400 W HPI lamps (Philips, Hamburg, Germany) and 400 W SON-T lamps (Philips) alternating every 2 h with 5 min overlap giving a PAR light intensity between 350 and 450 μmol m^{-2} s^{-1} at canopy level. Common bean (*Phaseolus vulgaris* L. cv Fardenlosa Shiny) was sown in a potting soil (ED 73; Einheitserde, Fröndenberg, Germany) and repotted into the soil mix after three days. The plants were grown in a greenhouse during February and March with a day/night regime of 26/18°C and 45/80% relative humidity, respectively. High-pressure sodium lamps ensured a photoperiod of 16 h and that light intensity never fell below a PAR value of about 390 μmol m^{-2} s^{-1}.

Harvests and Measurement of Root Parameters

For destructive analysis, the soil column was pushed out of the tube by removing the bottom of the pot and inserting a piston. Roots were carefully washed out of the soil with tap water. Fresh weights were measured on a balance (Sartorius, Göttingen, Germany) after carefully removing adhering water with paper towels. For root lengths measurement, the roots were transferred to a water bath where they were stored until scanning with WinRHIZO (Regent Instruments, Quebec City, Quebec, Canada).

MRI Measurements

All MRI measurements were performed on a 4.7 T magnet (Magnex, Oxford, UK) with a vertical bore (310 mm i.d.) and magnetic field gradient coils (205 mm i.d.) providing gradients of up to 300 mT/m. The vertical direction of the borehole allows plants to be measured in their natural upright position. Since the size of a radio-frequency coil affects the signal-to-noise ratio, we used a 64 mm i.d. coil (Varian, Palo Alto, CA), a 100 mm i.d. coil (Varian), or a 170 mm i.d. coil (Rapid, Würzburg, Germany) depending on sample size. The experimental control was run on a VNMRS console (Varian) that was connected to the software VnmrJ (Varian) running on a Linux PC. All root images were acquired using standard vendor-supplied MRI sequences, SEMS (Spin-Echo Multi-Slice), and SE3D (3D Spin-Echo) (Haacke et al., 1999). Gradient echo imaging was found unsuited for root imaging due to inhomogeneous fields caused by soil particles. For the larger (longer than 50 cm) and heavier (>10 kg) containers, a one-dimensional positioning system (Isel Germany, Eichenzell, Germany) was placed on top of the magnet. By means of a pulley and a custom-built sample guidance system inside the gradient bore, objects with lengths up to 150 cm could be measured (Fig. 1E). The positioning system was controlled by LabVIEW (National Instruments, Austin, TX) procedures and integrated into the Varian console via Python (Python Software Foundation, Beaverton, OR) routines and VnmrJ (Varian) macros. Smaller samples were positioned by an industrial pick-and-place robot (Mini-Liner 3.0 Alu; Geiger Handling, Dornhan, Germany) mounted on top of the magnet. The robot was controlled by a LabVIEW program (National Instruments) to pick up individual plants from a mounted rack and to place them inside the magnet. Python routines were used for passing commands from the VnmrJ software to the computer running LabVIEW (National Instruments). Integration of the control of the pick-and-place robot into the automated measurement protocols allowed the MRI spectrometer to run continuously without user intervention. Both positioning systems allowed the samples to slide up and down in borehole of the magnet, in order to do multiple scans in the vertical direction. Using a bar-code reader, MRI measurements were coupled to individual pots. Postacquisition data processing, including data reordering, filtering (flat-top Gaussian: $1.0 \times \exp(-(1/\delta^2)^4 \times \ln(2)0.4)$ $\delta = 0.56$ of k-space width), Fourier transformation, and concatenating data blocks was done with custom-made scripts written in IDL (ITT, Boulder, CO).

Image Data Analysis

Automated image analysis was performed using an in-house developed software tool, named NMRooting (available at http://www.nmrooting.de), which was written in the programming language Python and based on the software library described by Schulz et al. (2013). NMRooting utilizes Mayavi (Ramachandran and Varoquaux, 2011) for 3D visualization and Igraph (Csardi and Nepusz, 2006) as a graph network library. To calculate root traits from 3D MRI data, the software first extracts a morphological skeleton, which is defined by a list of connected voxels. To extract the skeleton, a mask was obtained through a combination of thresholding (six times the noise level of the MRI data) and dilation by 1.75 mm. All voxels outside the obtained mask were discarded from any further analysis. The dilation ensured that gaps up to 3.5 mm distance can be bridged by the algorithm. Connectivity of the remaining voxels was obtained by tracing the shortest path from each voxel above the threshold to the base of the shoot using Dijkstra's algorithm (Dijkstra, 1959). Here, the cost of a path was determined by the MRI signal and the distance transform of the root voxel segmentation, thus favoring paths running along voxels with high MRI signal as well as paths running in the center of the segmented root volume. All these paths are then joined together to form the morphological skeleton. The thus-obtained root structure (which in mathematical, morphological terms is a "tree") required "pruning" as it contains many, generally short, paths to adjacent voxels that were not roots. First, all voxels that were passed by fewer than five shortest paths were discarded from the morphological skeleton, eliminating already a large amount of unwanted voxels. After this step, however, multiple artificial side branches within single root segments remained. They were removed by discarding all side branches with a total length of <5 mm. Finally, the last pruning step considered paths crossing areas with a MRI signal below the threshold. Such MRI signal voids can occur, for example, due to small residual FMPs. The ability of the Dijkstra routine to close such gaps is one such feature; however, paths bridging gaps greater than 3.5 mm were considered artificial and removed from the morphological skeleton. The validity of the resulting skeleton was examined visually by overlaying them on the raw magnetic resonance images. From the resulting final skeleton, root traits such as root length, number of root tips, or root angles (referring to the horizontal plane) were calculated. Similar to Hargreaves et al. (2009), initial branching angles of the main axis were determined by the slope (degrees from horizontal) of a line that connects a manual chosen starting point at the base of the stem and the position of the roots 20 mm below that point. The calculations of the various traits were typically performed in less than 5 min per root system on a single core. This short processing time also allowed for a quick sensitivity analysis of the traits to the chosen image processing parameters.

Total fresh weight of the roots was estimated using the MRI signal intensity. As the soil water signal was below the noise level, Eq. 1 shows that the resulting MRI signal is proportional to the root water content in a given voxel. The calibration constant K (16 a.u. mm^{-3}) was corrected for an average root water relaxation time $T_{2,\mathrm{root}}$ (here we used 25 ms). The total root mass was then calculated by summing up the signal intensity of all voxels above the 6*noise threshold to avoid adding false positives that increase exponentially with lower threshold.

Root diameters were estimated by calculating the local root mass of 10-mm-long root segments. The segment mass estimate was based on all voxels within 1 mm from the root segments center. Assuming a root segment can be approximated by a homogeneously filled cylinder, the average diameter d of a segment is: $d = \frac{1}{2}\sqrt{\frac{m}{L\pi\rho_{\mathrm{H_2O}}}}$ with m the segment mass, and L the segment length (here: 10 mm). This method may underestimate the root diameter when air spaces, such as root cortical aerenchyma or other anatomical features, reduce NMR signal intensity. Mean diameters of a root system are calculated by averaging the obtained root diameters over the root segments.

Based on MRI data, growth rates, increase in root mass, and numbers of tips were calculated from linear regressions fitted to the data for each plant. Assuming linear growth, the slope of this regression gives the individual growth rate for each plant. The mean growth rate for all plants of the same species is presented here.

Angular projections of various root traits were calculated by converting the Cartesian x,y,z grid to a cylindrical r,ϕ,z grid (here, ϕ equals the angle in the horizontal plane), using $r^2 = (x-x_0)^2 + (y-y_0)^2$, with x_0 and y_0 either representing the middle of the pot or the position of the shoot. The dimensionality of the data set can be reduced by integration of the angle, ϕ, such that one obtains a 2D r,z image. Figure 6, A and B, illustrates how the angular projections were achieved and what the 2D distribution of different root traits looks like (Fig. 6, E, G, J, L, and N). Further data reduction was obtained by calculating trait values in horizontal planes that were each 5 mm thick and displayed as one-dimensional depth profiles (Fig. 6, F, H, K, M, and O). Here, for root mass, root length, and root tips, the values in each horizontal plane were summed up while, for mean root angles and diameters, the values were averaged over the root length.

For comparison with the described automated NMRooting routine, manual root tracking was also performed (see Supplemental Fig. S1) by using home-built procedures implemented in MeVisLab (MeVis Medical Solutions AG, Bremen, Germany) and MATLAB (The MathWorks, Natick, MA). The individual roots were tracked manually by visual inspection of 2D maximum intensity projections in three orthogonal planes and 3D volume rendering of the data. This procedure resulted in sets of 3D coordinate sequences from which the number of roots, their individual length, and the sum of the root lengths (i.e. total root lengths) were derived.

Supplemental Data

The following supplemental materials are available.

Supplemental Figure S1. Comparison of root length of six barley plants at six time points.

Supplemental Figure S2. Root length per diameter classes.

Supplemental Figure S3. Development of root length per root diameter class.

ACKNOWLEDGMENTS

The authors gratefully acknowledge the help of Esther Breuer for assisting in root lengths determination.

Received September 8, 2015; revised December 2, 2015; accepted December 29, 2015; published January 4, 2016.

LITERATURE CITED

Amato M, Pardo A (1994) Root length and biomass losses during sample preparation with different screen mesh sizes. Plant Soil **161:** 299–303

Asseng LAG, Aylmore JS, MacFall JR, Hopmans JW, Gregory PJ (2000) Computer-assisted tomography and magnetic resonance imaging. *In* AL Smit, AG Bengough, C Engels, M van Noordwijk, S Pellerin, SC van de Geijn, eds, Root Methods—A Handbook. Springer, Berlin, Germany, pp 343–364

Bashan Y, de-Bashan LE (2005) Fresh-weight measurements of roots provide inaccurate estimates of the effects of plant growth-promoting bacteria on root growth: a critical examination. Soil Biol Biochem **37:** 1795–1804

Bengough AG, McKenzie BM, Hallett PD, Valentine TA (2011) Root elongation, water stress, and mechanical impedance: a review of limiting stresses and beneficial root tip traits. J Exp Bot **62:** 59–68

Blümler P, Windt CW, van Dusschoten D (2009) Magnetic resonance in plants. Nova Acta Leopold **357:** 17–30

Borisjuk L, Rolletschek H, Neuberger T (2012) Surveying the plant's world by magnetic resonance imaging. Plant J **70:** 129–146

Box JE (1996) Modern methods for root investigation. *In* Y Waisel, A Eshel, U Kafkafi, eds, Plant Roots—The Hidden Half, 2nd Ed, Marcel Dekker, New York, pp 193–237

Brown DP, Pratum TK, Bledsoe C, Ford ED, Cothern JS, Perry D (1991) Noninvasive studies of conifer roots: nuclear magnetic resonance (NMR) imaging of Douglas-fir seedlings. Can J Res **21:** 1559–1566

Callaghan PT (1993) Principles of Nuclear Magnetic Resonance Microscopy. Oxford University Press, New York.

Chen YL, Dunbabin VM, Postma JA, Diggle AJ, Palta JA, Lynch JP, Siddique KHM, Rengel Z (2011) Phenotypic variability and modelling of root structure of wild Lupinus angustifolius genotypes. Plant Soil **348:** 345–364

Chimungu JG, Loades KW, Lynch JP (2015) Root anatomical phenes predict root penetration ability and biomechanical properties in maize (Zea Mays). J Exp Bot **66:** 3151–3162

Colombi T, Kirchgessner N, Le Marie CA, York LM, Lynch JP, Hund A (2015) Next generation shovelomics: set up a tent and REST. Plant Soil **388:** 1–20

Csárdi G, Nepusz T (2006) The Igraph software package for complex network research. InterJournal Complex Syst **1695:** 1–9

Dijkstra EW (1959) A note on two problems in connexion with graphs. Numer Math **1:** 269–271

Dorst L, Smeulders AWM (1987) Length estimators for digitized contours. Comput Vis Graph Image Process **40:** 311–333

Flavel RJ, Guppy CN, Tighe M, Watt M, McNeill A, Young IM (2012) Non-destructive quantification of cereal roots in soil using high-resolution x-ray tomography. J Exp Bot **63:** 2503–2511

Forde BG (2009) Is it good noise? The role of developmental instability in the shaping of a root system. J Exp Bot **60:** 3989–4002

Gregory PJ, Hutchison DJ, Read DB, Jenneson PM, Gilboy WB, Morton EJ (2003) Non-invasive imaging of roots with high resolution x-ray micro-tomography. Plant Soil **255:** 351–359

Gruwel MLH (2014) In situ magnetic resonance imaging of plant roots. Vadose Zone J **13:** 1–8

Haacke EM, Brown RW, Thompson MR, Venkatesan R (1999) Magnetic Resonance Imaging. John Wiley and Sons, New York

Hargreaves CE, Gregory PJ, Bengough AG (2009) Measuring root traits in barley (Hordeum vulgare ssp vulgare and ssp spontaneum) seedlings using gel chambers, soil sacs and x-ray microtomography. Plant Soil **316:** 285–297

Herdel K, Schmidt P, Feil R, Mohr A, Schurr U (2001) Dynamics of concentrations and nutrient fluxes in the xylem of Ricinus communis—diurnal course, impact of nutrient availability and nutrient uptake. Plant Cell Environ **24:** 41–52

Hillnhütter C, Sikora RA, Oerke EC, van Dusschoten D (2012) Nuclear magnetic resonance: a tool for imaging belowground damage caused by Heterodera schachtii and Rhizoctonia solani on sugar beet. J Exp Bot **63:** 319–327

Himmelbauer ML, Loiskandl W, Kastanek F (2004) Estimating length, average diameter and surface area of roots using two different image analyses systems. Plant Soil **260:** 111–120

Hochholdinger F (2009) The maize root system: morphology, anatomy and genetics. *In* JL Bennetzen, SC Hake, eds, Handbook of Maize: Its Biology. Springer Science + Business Media, New York, pp 145–160

Iyer-Pascuzzi AS, Symonova O, Mileyko Y, Hao Y, Belcher H, Harer J, Weitz JS, Benfey PN (2010) Imaging and analysis platform for automatic phenotyping and trait ranking of plant root systems. Plant Physiol **152:** 1148–1157

Jahnke S, Menzel MI, van Dusschoten D, Roeb GW, Bühler J, Minwuyelet S, Blümler P, Temperton VM, Hombach T, Streun M, Beer S, Khodaverdi M, et al (2009) Combined MRI-PET dissects dynamic changes in plant structures and functions. Plant J **59:** 634–644

Jassogne L, Hettiarachchi G, Chittleborough D, McNeill A (2009) Distribution and speciation of nutrient elements around micropores. Soil Sci Soc Am J **73:** 1319–1326

Kirby JM, Bengough AG (2002) Influence of soil strength on root growth: experiments and analysis using a critical-state model. Eur J Soil Sci **53:** 119–127

Köckenberger W, De Panfilis C, Santoro D, Dahiya P, Rawsthorne S (2004) High resolution NMR microscopy of plants and fungi. J Microsc **214:** 182–189

Koebernick N, Weller U, Huber K, Schluter S, Vogel HJ, Jahn R, Vereecken H, Vetterlein D (2014) In situ visualization and quantification of three-dimensional root system architecture and growth using x-ray computed tomography. Vadose Zone J **13:** 1–8

Kuchenbuch RO, Ingram KT, Buczko U (2006) Effects of decreasing soil water content on seminal and lateral roots of young maize plants. J Plant Nutr Soil Sci **169:** 841–848

Le Marié C, Kirchgessner N, Marschall D, Walter A, Hund A (2014) Rhizoslides: paper-based growth system for non-destructive, high throughput phenotyping of root development by means of image analysis. Plant Methods **10:** 13

Lynch JP (2007) Roots of the second green revolution. Aust J Bot **55:** 493–512

Lynch JP (2013) Steep, cheap and deep: an ideotype to optimize water and N acquisition by maize root systems. Ann Bot (Lond) **112:** 347–357

MacFall JS, Johnson GA (2012) Plants, seeds, roots, and soils as applications of magnetic resonance microscopy. *In* Encyclopedia of Magnetic Resonance. John Wiley & Sons, New York

Mairhofer S, Zappala S, Tracy SR, Sturrock C, Bennett MJ, Mooney SJ, Pridmore TP (2013) Recovering complete plant root system architectures from soil via x-ray μ-computed tomography. Plant Methods **9:** 8

Mairhofer S, Zappala S, Tracy SR, Sturrock C, Bennett MJ, Mooney SJ, Pridmore TP (2012) RooTrak: automated recovery of three-dimensional plant root architecture in soil from x-ray microcomputed tomography images using visual tracking. Plant Physiol **158:** 561–569

Metzner R, Eggert A, van Dusschoten D, Pflugfelder D, Gerth S, Schurr U, Uhlmann N, Jahnke S (2015) Direct comparison of MRI and x-ray CT technologies for 3D imaging of root systems in soil: potential and challenges for root trait quantification. Plant Methods **11:** 17

Metzner R, van Dusschoten D, Bühler J, Schurr U, Jahnke S (2014) Belowground plant development measured with magnetic resonance imaging (MRI): exploiting the potential for non-invasive trait quantification using sugar beet as a proxy. Front Plant Sci **5:** 469

Mitchell J, Chandrasekera TC, Gladden LF (2010) Obtaining true transverse relaxation time distributions in high-field NMR measurements of saturated porous media: removing the influence of internal gradients. J Chem Phys **132:** 244705

Mooney SJ, Pridmore TP, Helliwell J, Bennett MJ (2012) Developing x-ray computed tomography to non-invasively image 3-D root systems architecture in soil. Plant Soil **352:** 1–22

Moradi AB, Conesa HM, Robinson B, Lehmann E, Kuehne G, Kaestner A, Oswald S, Schulin R (2009) Neutron radiography as a tool for revealing root development in soil: capabilities and limitations. Plant Soil **318:** 243–255

Nagel KA, Kastenholz B, Jahnke S, van Dusschoten D, Aach T, Mühlich M, Truhn D, Scharr H, Terjung S, Walter A, Schurr U (2009) Temperature responses of roots: impact on growth, root system architecture and implications for phenotyping. Funct Plant Biol **36:** 947–959

Pohlmeier A, Haber-Pohlmeier S, Stapf S (2009) A fast field cycling nuclear magnetic resonance relaxometry study of natural soils. Vadose Zone J **8:** 735–742

Poorter H, Bühler J, van Dusschoten D, Climent J, Postma JA (2012) Pot size matters: a meta-analysis of the effects of rooting volume on plant growth. Funct Plant Biol **39:** 839–850

Postma JA, Dathe A, Lynch JP (2014) The optimal lateral root branching density for maize depends on nitrogen and phosphorus availability. Plant Physiol **166:** 590–602

Ramachandran P, Varoquaux G (2011) Mayavi: 3D visualization of scientific data. Comput Sci Eng **13:** 40–51

Rogers HH, Bottomley PA (1987) *In situ* nuclear magnetic resonance imaging of roots—influence of soil type, ferromagnetic particle content and soil water. Agron J **79:** 957–965

Schenck JF (1996) The role of magnetic susceptibility in magnetic resonance imaging: MRI magnetic compatibility of the first and second kinds. Med Phys **23:** 815–850

Schmittgen S, Metzner R, van Dusschoten D, Jansen M, Fiorani F, Jahnke S, Rascher U, Schurr U (2015) Magnetic resonance imaging of sugar beet taproots in soil reveals growth reduction and morphological changes during foliar *Cercospora beticola* infestation. J Exp Bot **66:** 5543–5553

Schulz H, Postma JA, van Dusschoten D, Scharr H, Behnke S (2013) Plant root system analysis from MRI images. *In* G Csurka, M Kraus, R Laramee, P Richard, J Braz, eds, Computer Vision, Imaging and Computer Graphics. Theory and Application, Vol 359. Springer, Berlin, Germany, pp 411–425

Stingaciu L, Schulz H, Pohlmeier A, Behnke S, Zilken H, Javaux M, Vereecken H (2013) In situ root system architecture extraction from magnetic resonance imaging for water uptake modeling. Vadose Zone J **12:** 1–9

Trachsel S, Kaeppler SM, Brown KM, Lynch JP (2013) Maize root growth angles become steeper under low N conditions. Field Crops Res **140:** 18–31

Trachsel S, Kaeppler SM, Brown KM, Lynch JP (2011) Shovelomics: high throughput phenotyping of maize (Zea mays L.) root architecture in the field. Plant Soil **341:** 75–87

Trachsel S, Stamp P, Hund A (2010) Effect of high temperatures, drought and aluminum toxicity on root growth of tropical maize (Zea Mays L.) seedlings. Maydica **55:** 249–260

van As H, Scheenen T, Vergeldt FJ (2009) MRI of intact plants. Photosynth Res **102:** 213–222

Vlamis J, Williams DE (1970) Comparative accumulation of Manganese and Boron in Barley tissues. Plant Soil **33:** 623–628

Wasson AP, Richards RA, Chatrath R, Misra SC, Prasad SVS, Rebetzke GJ, Kirkegaard JA, Christopher J, Watt M (2012) Traits and selection strategies to improve root systems and water uptake in water-limited wheat crops. J Exp Bot **63:** 3485–3498

Zobel RW (2008) Hardware and software efficacy in assessment of fine root diameter distributions. Comput Electron Agric **60:** 178–189

Zobel RW, Kinraide TB, Baligar VC (2007) Fine root diameters can change in response to changes in nutrient concentrations. Plant Soil **297:** 243–254